Enhanced selective photocatalytic oxidation of a bio-derived platform chemical with vacancy-induced core-shell anatase TiO$_2$ nanoparticles

Woo-Sung Jang [a,b,1], Vy Ngoc Pham [c,1], Sang-Hyeok Yang [a], Jaeyoon Baik [d], Hangil Lee [c,*], Young-Min Kim [a,b,**]

[a] Department of Energy Science, Sungkyunkwan University (SKKU), Suwon 16419, Republic of Korea
[b] Center for Integrated Nanostructure Physics, Institute for Basic Science (IBS), Suwon 16419, Republic of Korea
[c] Department of Chemistry, Sookmyung Women's University, Seoul 04310, Republic of Korea
[d] Beamline Research Division, Pohang Accelerator Laboratory (PAL), Pohang 37673, Republic of Korea

ARTICLE INFO

ABSTRACT

2,5-Furandicarboxylic acid (FDCA), a biodegradable alternative to fossil fuels, can be obtained via the catalytic oxidation of 2,5-hydroxymethlyfurfural (HMF), which is sourced from biomass. Anatase TiO$_2$ nanoparticles (NPs) with oxygen vacancies (V$_o$) effectively promote the oxidation process under ultraviolet/visible-light illumination. The conversion process is accelerated by introducing anatase TiO$_2$ NPs with a V$_o$-densified shell and stoichiometric core, which is achieved by a simple base treatment after synthesis. The defective shell acts as an electron-rich catalytic platform to facilitate HMF oxidation. Base-treated NPs measuring less than 20 nm yield ~40% conversion to FDCA via HMF oxidation at room temperature in water. The photocatalytic activity is achieved at a 580% higher rate than with the corresponding untreated TiO$_2$. Spectroscopic characterizations clearly visualize the densified layer of V$_o$ enclosing the surface of the high-performance TiO$_2$ NPs. Our results provide new insights into the optimal defect engineering of oxide-based catalysts for efficient biomass conversions.

1. Introduction

The oxidation of biomass materials using metal oxide (MO) nanoparticles (NPs) has recently attracted considerable interest owing to the high catalytic activity and selectivity of the NPs, which enable the production of valuable environmentally non-polluting chemicals and alternative fuels [1–3]. In particular, the bio-based molecule 2, 5-hydroxymethlyfurfural (HMF) has garnered significant interest as a platform for the photocatalytic production of useful intermediate polymers [4]; however, to fully realize the potential of this platform, the development of innovative MO-based catalysts is required [5]. One such intermediate polymers, 2,5-furandicarboxylic acid (FDCA), which is obtained from the photocatalytic oxidation of HMF, is a promising alternative to petroleum-based chemicals for the synthesis of biodegradable products [6,7]. The US Department of Energy considers FDCA to be one of the top 12 value-added chemicals derived from biomass like HMF [8]. The selectivity between the oxidation of –OH or –CHO is as important as the catalytic activity; hence, anatase TiO$_2$ is widely used as a catalytic support in combination with noble metals and their alloys, which selectively oxidize HMF to FDCA [2,9–12]. The eco-friendly and cost-effective production of FDCA requires the development of precious-metal-free catalysts that can work under base-free reaction conditions [6].

TiO$_2$ NPs have been employed as photocatalytic materials since the 1970s [13–15], and are among the most economically viable and environmentally sustainable catalysts [15]. Nonetheless, the present

catalytic performance of these materials barely meets the strict requirements of industrial applications. To improve the photocatalytic performance and efficiency of existing TiO_2 catalysts, engineering strategies to reduce the size of the NPs and introduce surface defects such as dopants and oxygen vacancies (V_o) have been adopted in the development of high-performance TiO_2-based catalysts [16–18]. The most efficient strategy is to modify the surface to increase the number of oxygen vacancies [19–21], because the defective surface exhibits higher catalytic activity toward oxidation [22–26].

Herein, we introduce highly efficient V_o-induced core-shell anatase TiO_2 NPs for the selective oxidation of HMF at room temperature in water. A V_o-densified shell was formed by the simple treatment of the as-synthesized anatase TiO_2 NPs with a basic solution. We previously reported that the defect density in TiO_2 NPs could be increased by the strong deprotonation effect that acts under a basic pH [26]. Under optimal basic treatment conditions (Section 2), V_o are highly concentrated within a 1–2 nm in thickness from the surface without altering the anatase lattice framework, thereby forming a defective shell ($TiO_{2-\delta}$, where δ is the oxygen deficiency), while retaining the stoichiometric anatase TiO_2 structure of the NP core. The untreated anatase TiO_2 NPs were compared with core-shell homostructured NPs of a similar size to decouple the size reduction effect from the contribution of the defect-charge interplay to the resulting photocatalytic activity. Core-shell NPs measuring less than 20 nm achieved the full oxidation of HMF, ~580% faster than untreated anatase TiO_2 NPs, and ultimately yielding ~40% conversion to FDCA. Multiscale spectroscopic characterization based on high-resolution x-ray photoelectron spectroscopy (HRXPS) and electron energy-loss spectroscopy (EELS) clearly detected and spatially mapped the densified shell of V_o surrounding the core of the NPs. The formed shell was defective and electron-rich, and thus catalyzed the oxidation of HMF. Atomic-resolution high-angle annular dark field scanning transmission electron microscopy (HAADF-STEM) confirmed the anatase structure of all the TiO_2 samples, regardless of the presence or absence of the defective shell, with no structural change observed below the outermost surface. Our results indicate that the enhanced photocatalytic activity of the core-shell NPs mainly results from the high density of vacancy-induced electrons populating the surface layer. Furthermore, the reduced size of the NPs increasing the surface area acts synergistically with the higher catalytic activity of the anatase structure to enhance the photocatalytic activity.

2. Experimental

2.1. Sample preparation

Anatase TiO_2 NPs were synthesized using an established method [27], in which the growth time was varied to yield NPs of various sizes. Titanium tetraisopropoxide (TTIP, 99.95%, Sigma–Aldrich), Titanium isopropoxide (TIP, 99.9%, Sigma–Aldrich), and anhydrous ethanol were used for the preparation of the titanium precursor and solvent. In detail, the TTIP of 2.0 g was introduced into a round-bottomed flask (100 ml) containing double distilled water (30 ml). The diluted TTIP solution was stirred (rpm = 100) for 30 min. The TIP of 5.0 g was separately diluted with anhydrous ethanol (5.0 g, 99.9%, DAEJUNG Co. Ltd.) and stirred (rpm = 100) for 30 min. The diluted TIP was added dropwise into the TTIP solution with vigorous stirring (rpm = 200) at room temperature. After that, a white TiO_2 precipitate was obtained. The size of the TiO_2 NPs was adjusted by varying the reaction time of the mixed solutions (denoted as TN-1 and TN-2). After fabricating the anatase TiO_2 NPs, the solution was prepared with the pristine TN-1 NPs of 3 g in water (100 ml) and then titrated using KOH (base) to the target pH of 13.0. The titrated solution was stirred (rpm = 80 rpm) for 3 h at 90 °C until homogenous mixing is obtained. The homogeneous solution was then transferred into sealed Teflon-lined autoclaves and heated at 220 °C for 9 h and finally stored in convection oven for drying for 48 h at 90 °C to obtain the base-treated TiO_2 NPs (labeled TN-4).

The base-treated NPs (TN-4) were subsequently annealed at 750 °C for 3 h in Ar atmosphere to yield larger NPs (labeled TN-3). The average sizes of the four samples were measured by low-magnification TEM imaging (Fig. S1). The resulting four TiO_2 NP samples (labeled TN-1, TN-2, TN-3, and TN-4) were filtered and washed with double-distilled water to remove any probable residues. All materials used in this study were purchased from Sigma–Aldrich. The BET surface area analysis of the four TiO_2 samples was performed under the N_2 adsorption isotherm at 77 K using Autosorb-iQ 2ST/MP (Quantachrome).

2.2. Photocatalytic oxidation

To evaluate the photocatalytic activity, four TiO_2 NP suspensions (0.5 g/L) containing HMF (25 mM) were stirred for 1 h in the dark to attain adsorption equilibrium. The reactor containing the TiO_2 NP solution was placed 10 cm in front of blue light-emitting diodes (LEDs, $\lambda = 365$ nm, output power = 6 W; Thorlab) under magnetic stirring at ~80 rpm. A 30 ml volume reactor with a quartz window of 40 mm in diameter was used for the photocatalytic test. All PCD experiments were conducted under air ambiance with the reactor kept open. The intensity of the blue LED (output power: 6 W) used in this study was measured using a calibrated optical power meter (1830-C, Newport). When the intensity was measured at the distance of 10 cm from the LED along the irradiation axis, the light intensity was determined to be 10 ± 0.7 mW/cm^2. During this process, aliquots (1 ml) of the suspension of each sample were extracted at different time intervals from 1 to 24 h and separated using a 0.45 μm Whatman filter. The HMF oxidation products were analyzed using HPLC-MS (ULTIMATE 3000 RSLC SYSTEM, Thermo Fisher Scientific and Q-EXACTIVE ORBITRAP PLUS MS, Thermo Fisher Scientific). For the LC analysis, two solvents (A: 6.5 mM ammonium bicarbonate in diluted water, B: 6.5 mM ammonium bicarbonate in acetonitrile) and InfinityLab poroshell HPH-C18 (2.15×150 mm, 4 μm, Agilent Technologies Korea Ltd) column at 45 °C were used. The flow, sample temperature, and injection volume were set to be 0.400 ml/min, 5 °C, and 5 μL, respectively. For MS measurement, the experimental conditions were set by the following parameters: full MS (70,000 resolution)-ddMS2 (17,500 resolution) (80–1000 m/z) scan type, negative polarity, 5 loop counts, 30 collision energy, 5.0 s dynamic exclusion, 50 sheath gas flow rate, 13 aux gas flow rate, 2.5 kV spray voltage, 263 °C capillary temperature, 50 S-lens RF level, and 425 °C aux gas heater temperature. Electron spin resonance (ESR, JES-X320, JEOL Ltd.) spectra of the four TiO_2 NPs were obtained from 300 to 400 mT at 300 K with a frequency of 9446 MHz, power of 10 mW, modulation frequency of 100 kHz, and width of 0.4 mT.

2.3. Structural and chemical characterizations

The X-ray diffraction (XRD) patterns of the four TiO_2 NP samples were acquired using a D8 Advance TRIO/TWIN diffractometer (Bruker, USA) with Ni-filtered Cu Kα radiation. The electronic structures of the Ti $2p$ and O $1s$ core levels of the four TiO_2 samples were analyzed using HRXPS at the 8A1 beamline of the Pohang Accelerator Laboratory. The morphologies and size distributions of the TiO_2 NPs were analyzed by high-resolution transmission electron microscopy (HRTEM, JEM-ARM200CF) at 200 kV. The atomic structures of the four TiO_2 NP samples were imaged using the HAADF imaging mode in the STEM. The angle range of the ADF detector was set to 68–280 mrad, while the probe angle was approximately 23 mrad. Nanoscale elemental maps of the four TiO_2 NP samples were obtained using energy-dispersive X-ray spectroscopy (EDX) with a double-silicon drift detector (JED-2300 T, JEOL Ltd.) with an effective solid angle of ~1.2 sr. EELS (Gatan GIF Quantum ER 965) in the STEM imaging mode was employed to obtain a core-loss EELS spectrum imaging (SI) dataset including the Ti $L_{2,3}$ and O K edges. The dimension and acquisition conditions in SI for the scanning probe-based EELS experiment were set to 69 × 69 pixels with a scanning step of 2.1 nm/pix and a scanning speed of 0.5 s/pix. The statistical noise

in the EELS SI datasets was filtered by applying principal component analysis using commercial software (MSA, HREM Research). To map the Ti valence state, multiple linear least-squares (MLLS) fitting was performed with the Ti $L_{2,3}$ edges acquired from the surface and core of an arbitrarily chosen NP in each EELS spectrum image of the four TiO$_2$ samples. The MLLS fitting software was implemented using microscope control software Gatan DigitalMicrograph®. Owing to the low intensities and small difference between the O K edges of the surface and the core of the TiO$_2$ NPs, MLLS fitting to the EELS SI dataset could not reliably differentiate the shapes of the O K edges with respect to V_o. To address this issue, the K-means clustering algorithm was applied to reconstruct the oxygen vacancy distribution maps from the reference spectral features extracted from the loading maps by non-negative matrix factorization (NMF). The experimental EELS SI datasets for the four TiO$_2$ samples were decomposed into four components by NMF decomposition as a function of their weight. The loading map and vector parameters were continuously updated using the gradient descent method with the Frobenius norm loss [28].

3. Results and discussion

3.1. Crystal structure and size distribution of anatase TiO$_2$ NPs

Two anatase TiO$_2$ samples were synthesized with average sizes of ~22 nm and ~16 nm (denoted as TN-1 (Fig. 1a) and TN-2 (Fig. 1d)) as counterpart reference samples. Core-shell TiO$_2$ NPs with an average size of ~16 nm were fabricated from TN-1 NPs (denoted as TN-4, Fig. 1j) via basic treatment, and further thermal annealing at 750 °C for 3 h increased the size of the core-shell TiO$_2$ NPs to an average of ~38 nm (denoted as TN-3, Fig. 1g). The morphologies and elemental distributions of the four samples were investigated using bright-field TEM and EDX. The TEM images (Fig. S1 in the supplementary material) reveal the irregular shapes and different size distributions of the samples (Fig. 1c, f,

i, and l). For reference, the results of BET surface area analysis for the four samples are listed in Table S1 in the supplementary material. Even though the average size of the TN-3 sample is more than twice that of the TN-4 sample, the surface areas are similarly measured due to the characteristically wide size distribution of the TN-3 sample, which contrasts with the TN-4 sample having a narrow distribution of particle sizes. Additionally, the EDX maps show that the Ti and O atoms are uniformly distributed throughout the NPs without artifact elements, confirming their elemental purity at the nanoscale (Fig. S2). XRD results revealed that all four samples had a monophasic crystal structure consisting of tetragonal anatase ($I4_1/amd$) [29], suggesting that the additional basic treatment and thermal annealing were ineffective in altering the initial crystal phase of the synthesized NPs (Fig. S3a). Furthermore, the XRD peaks of the TN-2 and TN-4 NPs were broader than those of the TN-1 and TN-3 NPs owing to the smaller particle sizes of the TN-2 and TN-4 NPs [30]. This result is consistent with the size distributions observed by TEM (Fig. S3b).

The atomic-scale crystal structure of the four TiO$_2$ NPs was confirmed by the HAADF-STEM imaging of the four samples oriented in the [100] crystallographic direction (Fig. 1a, d, g, and j), which clearly showed a lattice framework consisting of Ti atoms; however, O atoms were barely detected owing to the strong atomic number (Z) dependence of the signal intensity ($I \propto Z^{1.6-2}$) [31,32]. All the Ti atomic columns along the [100] orientation of the anatase structure were separately imaged and showed a typical array of Ti atomic dumbbells (atomic model on each STEM image). All the TiO$_2$ NPs exhibited a typical dumbbell array of Ti atoms that showed an excellent match with the atomic model of [100]-oriented anatase TiO$_2$. These results are consistent with those of macroscale XRD experiments. To confirm whether the structural integrity was maintained throughout the TiO$_2$ NPs, including the outermost surface, distance profiles were plotted by measuring the extended dumbbell spacing of Ti atoms from the core to the outermost surface of each NP (Fig. 1b, e, h, and k). No alteration of the
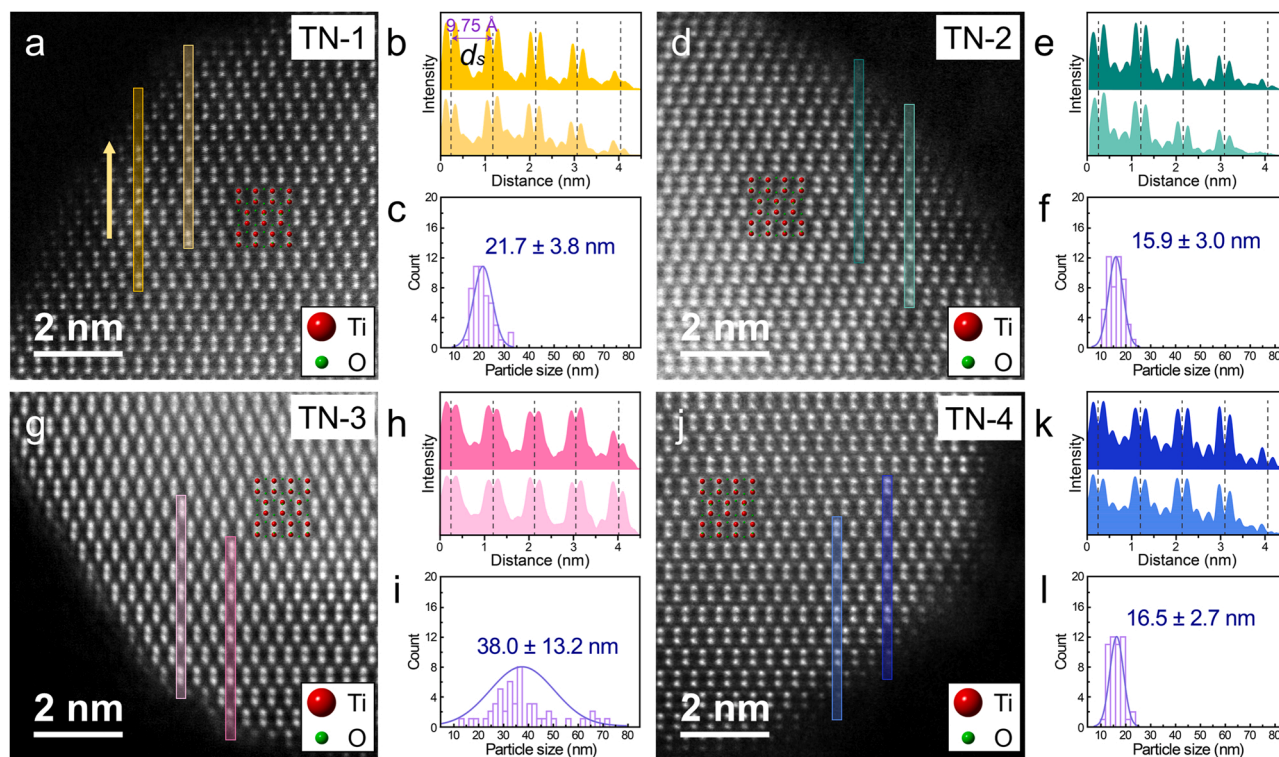
Fig. 1. Atomic-resolution HAADF-STEM images of (a) TN-1, (d) TN-2, (g) TN-3, and (j) TN-4 NPs. The overlaid atomic model on each image depicts [100]-oriented anatase TiO$_2$ ($I4_1/amd$). (b, e, h, k) Lattice spacing between Ti dumbbell moieties (d_s = 9.75 Å) along the [001] orientation in the anatase TN-1, TN-2, TN-3, and TN-4 NPs, respectively (vertical lines in each image). (c, f, i, l) Particle size distributions in the TN-1, TN-2, TN-3, and TN-4 samples, respectively. The size distributions were obtained from the low-magnification HRTEM images of those samples shown in Fig. S1.

characteristic spacing (d_s = 9.75 Å) between the Ti dumbbells along the [001] direction was observed in any of the TiO$_2$ NPs, demonstrating that the basic treatment and subsequent thermal annealing exerted no influence on the Ti lattice framework of the as-synthesized anatase TiO$_2$ NPs, and thus, did not affect their structural stability.

3.2. Macroscale spectroscopic analysis of defect distributions

Although all four TiO$_2$ samples were crystallographically and elementally identical, their electronic structures are expected to be different owing to the likely effect of basic pH treatment on the electronic structure of the TiO$_2$ NPs arising from the introduction of V$_o$ [26]. To clarify this issue, HRXPS profiles of the Ti 2p and O 1s core levels of the four TiO$_2$ samples with the morphological size differences were obtained (Fig. 2a). This characterization allowed the number of vacancy defects and relevant charge states of the transition metal to be estimated (Fig. 2b and c) [33–35]. The Ti 2p core-level spectra of the four samples (Fig. 2b) show a typical Ti 2$p_{3/2}$ peak corresponding to Ti^{4+} at 458.6 eV and another corresponding to the defect-induced state of Ti (Ti^{3+}) at a binding energy of 457.9 eV [35–38]. The intensity of the latter peak is ascribed to the number of atomic defects; thus, the increasing intensity of this peak in the order of TN-4 >TN-3 >TN-2 >TN-1 suggests that the catalytic activity of TiO$_2$ is improved as the number of atomic defects increases.

Similarly, the O 1s core-level spectra of the TiO$_2$ samples elucidate the vacancy-induced defect states. The intensities of the peaks at 531.2 eV and 532.6 eV in the O 1s core-level spectrum are proportional to the V$_o$ and OH$^-$ contents of the sample, respectively (Fig. 2c) [32,33, 38]. Comparison of NPs with a similar average size (TN-2 and TN-4) shows that the concentration of V$_o$ is significantly increased by basic pH treatment. In addition, a direct comparison of untreated (TN-1 and TN-2) or treated (TN-3 and TN-4) samples confirms that reducing the size of the NPs increases the defect density. Nevertheless, the density of vacancy defects is clearly increased by basic pH treatment, even though the enlarged active surface area arising from the size reduction also contributes to an increase in the defect density. Untreated TN-2 with an average size of ~16 nm has a lower defect content than treated TN-3 with an average size of ~38 nm. These observed spectral features of

the O 1s edge of the four TiO$_2$ samples are well correlated with those of the Ti 2p core-level spectra. It is worth noting that bandgaps of the four TiO$_2$ NPs were similarly measured in macroscale UV-Vis diffuse reflectance spectroscopy analysis (Fig. S4). This result suggests the need for nanoscale spectroscopic analysis to elucidate how atomic defects are distributed on a single particle level.

Electron spin resonance (ESR) is a sensitive technique for the detection of the unpaired spin density resulting from the reduced states of transition metal ions [39]. Herein, the ESR signal becomes more structured as the number of reduced Ti^{3+} states increased with densification of V$_o$ [40,41]. Indeed, the ESR signal becomes shaper and stronger in the order of TN-4 >TN-3 >TN-2 >TN-1 (Fig. 2d), with the ESR profile of TN-4 showing a stronger and sharper peak structure than those of the others. A more intense peak at approximately 340 mT in the ESR spectra (denoted A, g = 2.00) indicates a higher number of V$_o$ [42]. In addition, the peak at approximately 350 mT (denoted B, g = 1.93) suggests that Ti^{3+} ions exist on the surface of the TiO$_2$ NPs [41]. Considering the ESR and HRXPS profiles of the four TiO$_2$ samples, the TN-4 NPs are expected to contain the largest amount of reduced Ti^{3+} ions and V$_o$ on the surface, and consequently demonstrate the highest photocatalytic activity. These spectroscopic results are supported by the photocurrent responses of the four TiO$_2$ samples (Fig. S5). The photocurrent density increases in the order of TN-1, TN-2, TN-3, and TN-4. Characteristically, the photocurrent densities of the treated TiO$_2$ samples (TN-3 and TN-4) are higher than those of pristine TiO$_2$ samples (TN-1 and TN-2), implying that atomic defects would be intensified on the surface of the base-treated TiO$_2$ NPs.

3.3. Photocatalytic oxidation of HMF

The photocatalytic degradation (PCD) activities of the modified TiO$_2$ NPs for HMF oxidation were monitored as a function of the ultraviolet (UV) illumination time to compare their photocatalytic functionalities. The 24 h PCD profiles of the samples (Fig. 3a) show that the decomposition efficiency of the base-treated TN-4 NPs is superior to that of the other samples; almost all of the HMF content is decomposed by the TN-4 NPs in 24 h, while the other catalyst samples do not achieve the complete oxidation of HMF. The photocatalytic performance is also
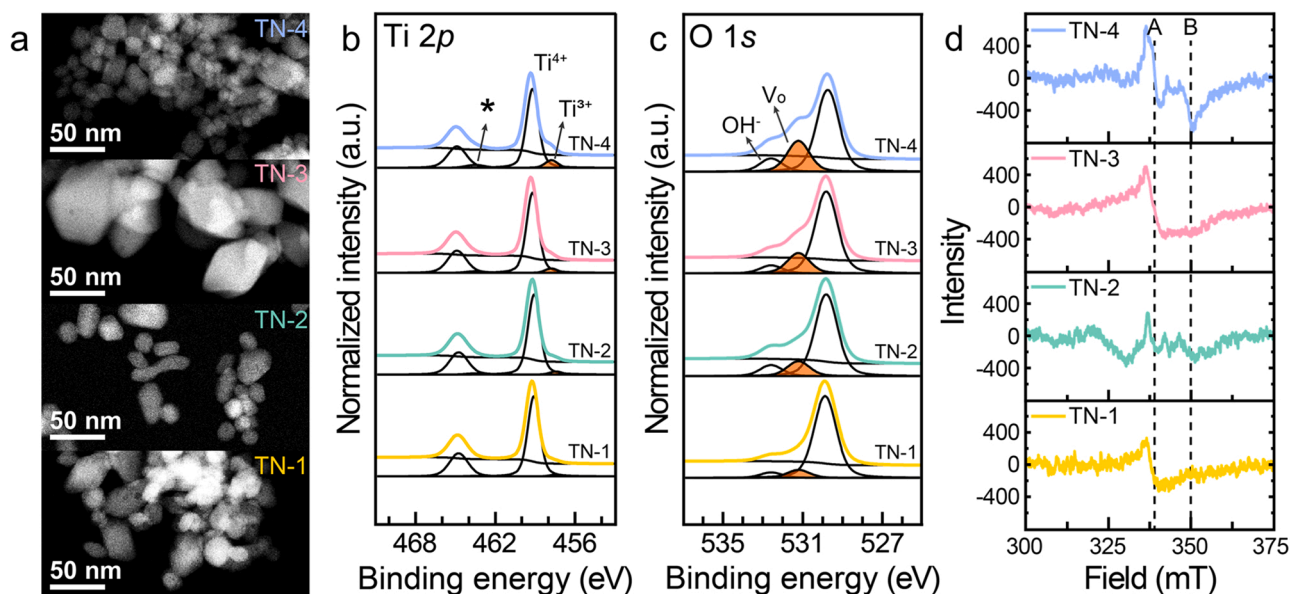
Fig. 2. (a) Morphologies of TN-1, TN-2, TN-3, and TN-4 NPs. HRXPS profiles of the (b) Ti 2p and (c) O 1s core levels of TN-1, TN-2, TN-3, and TN-4 TiO$_2$ NPs. Orange-shaded areas represent the densities of Ti^{3+}-reduced states and V$_o$ in each spectrum. (d) ESR spectra of the four samples. The peaks at A (~340 mT) and B (~350 mT) are the resonance peaks arising from the presence of an unpaired spin density, which is strongly correlated with the HRXPS profiles that show the evolution of the reduced states of Ti ions. Note that the weak peak denoted by the asterisk indicates Ti^{3+} 2$p_{1/2}$ peak (463.6 eV), while the peak marked with Ti^{3+} points to Ti^{3+} 2$p_{3/2}$ peak (457.9 eV).
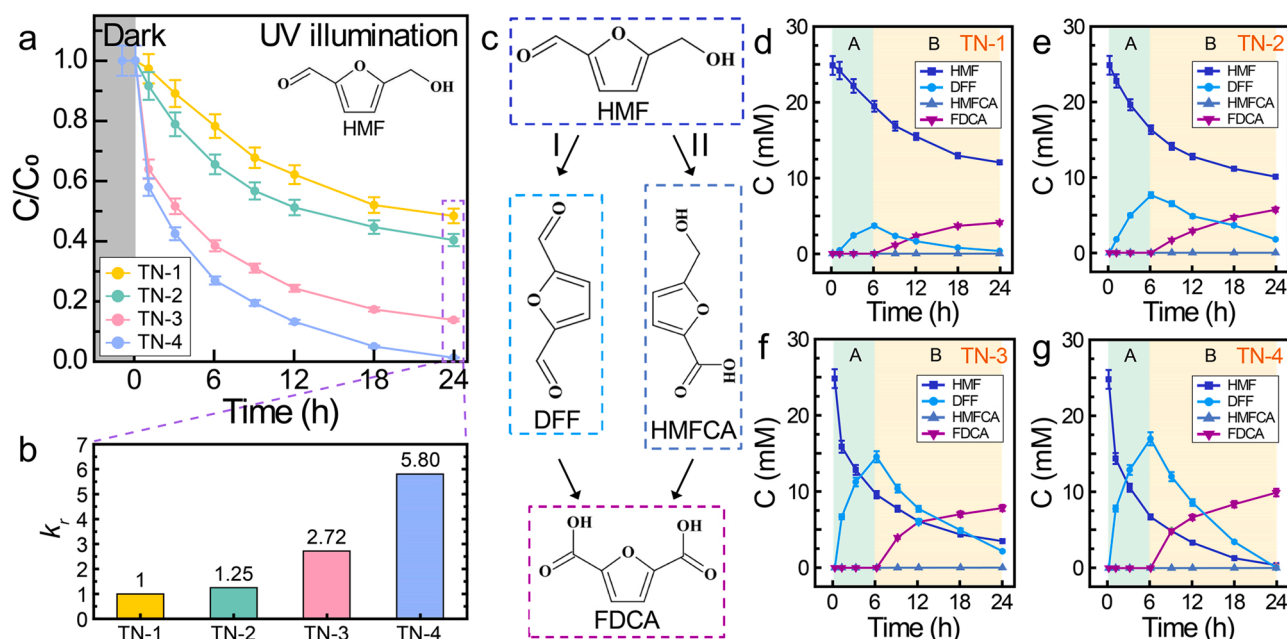
Fig. 3. (a) Photocatalytic decomposition profiles of HMF using the four TiO$_2$ NPs under UV illumination ($\lambda = 365$ nm). (b) Relative reaction rate constant (k_r) of the size-reduced and the base-treated TiO$_2$ NP samples compared with that of the pristine TN-1 sample after 24 h of UV irradiation. (c) Possible reaction pathways, I and II, of FDCA production via HMF oxidation. (d–g) Concentration profiles obtained from the LC-MS of the oxidative reaction of HMF with (b) TN-1, (c) TN-2, (d) TN-3, and (e) TN-4 NPs.

improved in the order of TN-4 >TN-3 >TN-2 >TN-1, which is consistent with the prediction drawn from the macroscale spectroscopic analysis. To assess the mechanism by which the photocatalytic performance was enhanced, the rate constants (k_r) of the samples were compared to that of the TN-1 sample after 24 h of the reaction (Fig. 3b). The rate constant for the oxidation of HMF by the base-treated TN-4 NPs is 5.8 times greater than that for the oxidation of HMF by the TN-1 NPs. The base-treated TN-3 NPs, despite having the largest average size (~38 nm), show 2.72 times higher catalytic performance than the untreated TN-1 NPs that are almost half the size (~22 nm). This result suggests that engineering the surface defect structure is critical for the realization of high-performance catalysts. The photocatalytic activity of the base-treated TiO$_2$ NPs was demonstrated to be well sustained by more than 97% after five re-uses, indicating the robustness of the photocatalytic properties of the treated TiO$_2$ NPs in repetitive use (Fig. S6). A comparison of the HRXPS measurements of all TiO$_2$ samples before and after five cycling showed that the density of the reduced Ti^{3+} states was seldom changed (Fig. S7).

The reaction selectivity for the oxidation of –OH or –CHO in the synthesis of FDCA via the oxidation of HMF is as important as the catalytic activity. Therefore, identifying the functional groups that participate in the TiO$_2$-assisted oxidation of HMF is of crucial importance. Oxidation of the hydroxyl group and aldehyde yields 2,5-diformylfuran (DFF) or 5-hydroxymethyl-2-furancarboxylic acid (HMFCA), respectively, as an intermediate, which is then further oxidized to form FDCA. The selective oxidation of the –OH group (or –CHO group) in HMF forms the –CHO group (or –COOH group), DFF (or HMFCA), as an intermediate (Fig. 3c). Liquid chromatography-mass spectroscopy (LC-MS) was performed to identify the intermediate formed during HMF oxidation using anatase TiO$_2$ NPs. The raw LC-MS data of the four samples were given in Fig. S8. Fig. 3d–g shows the intermediates formed and consumed to form FDCA during HMF oxidation using TN-1, TN-2, TN-3, and TN-4. The concentration profiles indicate that the formation of FDCA occurs in two distinct stages: A and B. In stage A, the initial selective oxidation of HMF occurs over the first 6 h to form either DFF or HMFCA. In the subsequent stage B, which occurs from 6 h to 24 h, further oxidation of the intermediate occurs alongside HMF oxidation to

form FDCA as the final product. The LC-MS plots reveal that the DFF content increases significantly during stage A for HMF oxidation with all four TiO$_2$ samples and then gradually decreases during stage B owing to the further oxidation of DFF to form FDCA. Thus, we determined that the –OH functional groups were preferentially oxidized during the oxidation of HMF using TiO$_2$ catalysts (path I, Fig. 3c) [2,3,43]. As a plausible mechanism of the HMF oxidation in vacancy-densified TiO$_2$ NPs dispersed in an aqueous solution, a reaction pathway from HMF to DFF proposed by Khan et al. [44] is noteworthy; For the base-treated TiO$_2$ NP with a high density of oxygen vacancies, the UV/Vis light irradiation efficiently activates the formation of the radical cation when the HMF adsorbed on the electron-rich surface of the TiO$_2$. Meanwhile, dissolved oxygen gaining an electron from the TiO$_2$ surface is converted to a superoxide radical anion. Then, the radical cation reacts with the superoxide radical anion and subsequently generates hydroperoxyl radical and alkenyl radical. Eventually, the hydroperoxyl radical draws a hydrogen atom from the alkenyl radical and forms the DFF and byproduct H$_2$O$_2$ that possibly react with electrons to produce a hydroxyl radical. The hydroxyl radical then reacts with the DFF to form the FDCA.

Even though FDCA was obtained using all four TiO$_2$ samples, the conversion rates from HMF to DFF to FDCA differed substantially, indicating that the various samples exhibited different photocatalytic efficiencies (Fig. 3d–g). The use of the base-treated NPs typically resulted in higher yields of FDCA than that obtained with the use of untreated NPs, which was expected based on the results presented in Fig. 3a, which reinforces the importance of surface defect engineering as a primary strategy to enhance the photocatalytic efficiency of oxide catalysts. Among the samples, the TN-4 NPs showed the highest efficiency in the conversion of HMF to FDCA, with more than 99% of HMF being oxidized within 24 h to produce FDCA in a conversion yield of ~40%, which is a sufficient yield for industrial use. These results demonstrate the viability of employing surface-modified TiO$_2$ NPs for the efficient production of petrochemical substitutes from industrially important biomass.

3.4. Ti valency and oxygen vacancy distribution mapping of TiO$_2$ NPs

Because the superior photocatalytic performance of the base-treated NPs is attributed to the change in the electronic structure of the surface induced by the injection of V_o, the structure of the electronically modified surface of the base-treated NPs should be examined. To resolve the characteristic skin layer at a single-NP level, high-resolution EELS SI of the four TiO$_2$ samples was conducted. This approach uses a highly sensitive scanning focused electron probe to detect the interplay between the chemical potential and electronic structure on the nanoscale [32,45–47], which may elucidate the fundamental role of surface-densified V_o in photocatalytic reactions.

The site-specific distribution of defects and related changes in the electronic structure of the individual TiO$_2$ NPs were obtained by the MLLS fitting [48] of the local spectra of Ti $L_{2,3}$ and O K edges that were acquired from the surface and core of each TiO$_2$ NP, yielding two Ti $L_{2,3}$ (or O K) maps of the surface and core of the four TiO$_2$ NPs. Fig. 4 shows representative spectra of the Ti $L_{2,3}$ and O K edges (left panel) and the resulting spectral phase maps (right panel) of the four TiO$_2$ NPs. The L_3 and L_2 spectral shapes of Ti^{4+} in anatase TiO$_2$ show a characteristic crystal field splitting of two peaks, t_{2g} and e_g [49–53]. Reducing the valence state by the injection of V_o, and thereby forming the reduced species Ti^{x+} (x = 2 or 3), causes the sharply split peak to merge into a single peak owing to a loss of crystal symmetry and to shift to a lower energy by approximately 0.75–1.3 eV owing to the formation of localized donor levels below the conduction band of Ti 3d orbitals [22,26]. Similarly, the O K-edge in the spectrum of stoichiometric anatase TiO$_2$ typically shows a doublet peak (t_{2g} and e_g) at ~529 eV, which results from the hybridization of Ti 3d and O 2p orbitals [51,54,55]. As the number of V_o or local defects increases, the doublet peak increasingly overlaps with a singlet peak [56]; thus, the profile shapes of the Ti $L_{2,3}$ and O K edges can be used as reliable fingerprints to evaluate the distribution of defects in TiO$_2$ NPs.

The TN-1 and TN-2 NPs exhibit the typical profiles of quadruplet Ti $L_{2,3}$ and doublet O K edges of anatase TiO$_2$ regardless of the location in the TiO$_2$ NP (left panel, Fig. 4a, b). The Ti $L_{2,3}$ and O K edges acquired from the surface (yellow arrow) and core (blue arrow) of the TiO$_2$ NPs show no discernable difference. This result indicates that the electronic structure of the nanoparticles in both samples remains unchanged. MLLS fitting of the local spectra of the Ti $L_{2,3}$ edges shows a uniform distribution of Ti^{4+} states (right panel, Fig. 4a, b). The resolution of our nanoscale valence state mapping is barely sufficient to resolve the inherent defect states of the outermost surface; nevertheless, certain conclusions can be drawn. In comparison with the TN-1 NPs, the slight improvement in the photocatalytic activity of the TN-2 NPs is mainly ascribed to size reduction (Fig. 3). In contrast, characteristic doublet Ti $L_{2,3}$ and singlet O K edges are observed on the surface of TiO$_2$ NPs in the base-treated samples TN-3 and TN-4, whereas typical quadruplet Ti $L_{2,3}$ and doublet O K edges of anatase TiO$_2$ are observed for the core of the TiO$_2$ NPs (left panel, Fig. 4c, d). Moreover, the doublet Ti $L_{2,3}$ spectra of the surface of the base-treated samples are shifted to a lower energy by 1.3 eV. These results confirm that the reduced valence state of Ti^{x+} is extensively formed on the surface of TiO$_2$ NPs owing to the injection of a high concentration of V_o. MLLS fitting with two distinctive spectra of Ti atoms clearly resolves the two different valence states of Ti^{x+} and Ti^{4+} at the single-NP level (right panel, Fig. 4c, d). The corresponding V_o distribution maps confirm the high density of V_o on the surface, eventually inducing the reduced state of Ti atoms formed to achieve charge balance (Fig. S9). This nanoscale spectroscopic mapping of the Ti valency and V_o distribution directly resolves the stoichiometric cores and defective shells with a high density of V_o in the anatase TiO$_2$ NPs and unequivocally explains the difference in the macroscale HRXPS profiles of the untreated and base-treated TiO$_2$ NPs (Fig. 2). Our nanoscale characterization therefore elucidates the importance of defect engineering to
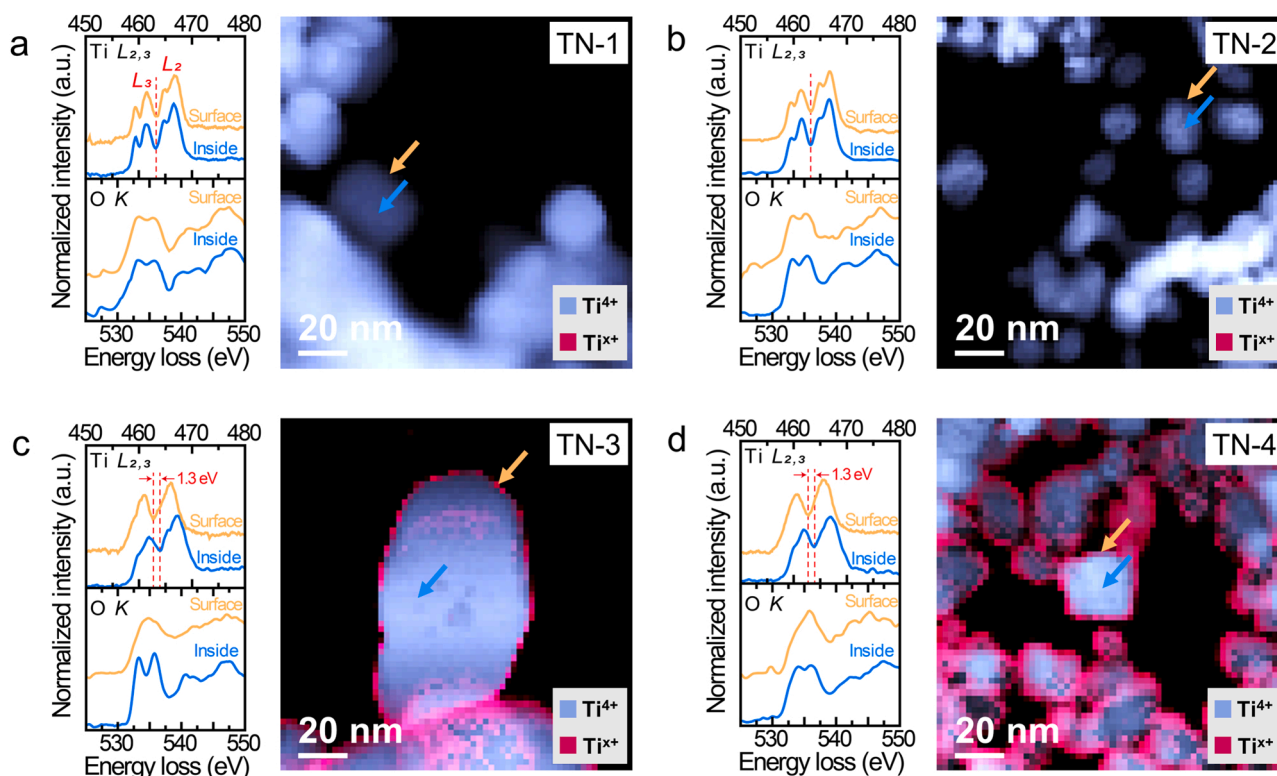
Fig. 4. (a–d) (left) Representative Ti $L_{2,3}$ and O K edges acquired from the surface (orange arrow) and core (blue arrow) of the four TiO$_2$ samples. (right) Composite spectral phase map of the stoichiometric Ti^{4+} (light blue) and reduced Ti^{x+} (magenta, x = 2 or 3) valence state maps of the four TiO$_2$ samples. The difference in the O K edges of the Ti^{2+} and Ti^{3+} samples is indistinct owing to the insufficient energy resolution of the EELS instrument. The Ti valence state maps were reconstructed by MLLS fitting to the experimental EELS SI with representative Ti $L_{2,3}$ edges corresponding to the surface and core of an arbitrarily selected TiO$_2$ NP.

create surface-active sites to enhance the photocatalytic oxidation of HMF, which can be achieved by facile base treatment.

4. Conclusions

Multiscale structural and chemical analyses clarified that the simple base treatment of anatase TiO_2 NPs induces the formation of a high concentration of V_O on the NP surface without altering the lattice structure, resulting in a distinctive V_O-densified shell and stoichiometric core homostructure. The formation of this electron-rich shell is advantageous for photocatalytic reactions; thus, the photocatalytic activities of core-shell NPs are expected to improve considerably. Indeed, in conjunction with the size reduction to ~16 nm, base treatment of the anatase TiO_2 NPs resulted in a remarkable synergistic improvement in the photocatalytic activity by ~580% relative to that of the untreated TiO_2 counterpart in the oxidation of biomass HMF. The photocatalytic oxidation of HMF followed a sequential oxidation pathway of HMF–DFF–FDCA. The yield of the alternative fuel FDCA reached ~40% after the complete consumption of HMF. Our results represent an important advancement in the development of cost-effective, eco-friendly alternatives to petrochemical materials via the facile defect engineering of catalyst oxides without noble metal additives.

CRediT authorship contribution statement

Declaration of Competing Interest

The authors declare that they have no known competing financial interests or personal relationships that could have appeared to influence the work reported in this paper.

Data availability

Data will be made available on request.

Acknowledgements

Appendix A. Supporting information

Supplementary data associated with this article can be found in the online version at doi:10.1016/j.apcatb.2022.122140.

References

[1] A. Lolli, V. Maslova, D. Bonincontro, F. Basile, S. Ortelli, S. Albonetti, Selective oxidation of HMF via catalytic and photocatalytic processes using metal-supported catalysts, Molecules 23 (2018) 2792, https://doi.org/10.3390/molecules23112792.

[2] A. Allegri, V. Maslova, M. Blosi, A.L. Costa, S. Ortelli, F. Basile, S. Albonetti, Photocatalytic oxidation of hmf under solar irradiation: coupling of microemulsion and lyophilization to obtain innovative TiO_2-based materials, Molecules 25 (2020) 5225, https://doi.org/10.3390/molecules25225225.

[3] A. Ulyankina, S. Mitchenko, N. Smirnova, Selective photocatalytic oxidation of 5-HMF in water over electrochemically synthesized TiO_2 nanoparticles, Process 8 (2020) 647, https://doi.org/10.3390/pr8060647.

[4] A. Tirsoaga, M. El Fergani, N. Nuns, P. Simon, P. Granger, V.I. Parvulescu, S. M. Coman, Multifunctional nanocomposites with non-precious metals and magnetic core for 5-HMF oxidation to FDCA, Appl. Catal. B: Environ. 278 (2020) 119309, https://doi.org/10.1016/j.apcatb.2020.119309.

[5] B. Zhu, C. Chen, L. Huai, Z. Zhou, L. Wang, J. Zhang, 2,5-Bis(hydroxymethyl)furan: a new alternative to HMF for simultaneously electrocatalytic production of FDCA and H_2 over CoOOH/Ni electrodes, Appl. Catal. B: Environ. 297 (2021), 120396, https://doi.org/10.1016/j.apcatb.2021.120396.

[6] C. Chen, L. Wang, B. Zhu, Z. Zhou, S.I. El-Hout, J. Yang, J. Zhang, 2,5-Furandicarboxylic acid production via catalytic oxidation of 5-hydroxymethylfurfural: Catalysts, processes and reaction mechanism, J. Energy Chem. 54 (2021) 528–554, https://doi.org/10.1016/j.jechem.2020.05.068.

[7] M.G. Davidson, S. Elgie, S. Parsons, T.J. Young, Production of HMF, FDCA and their derived products: a review of life cycle assessment (LCA) and techno-economic analysis (TEA) studies, Green. Chem. 23 (2021) 3154–3171, https://doi.org/10.1039/D1GC00721A.

[8] J.J. Bozell, G.R. Petersen, Technology development for the production of biobased products from biorefinery carbohydrates—the US Department of Energy's "Top 10″ revisited, Green. Chem. 12 (2010) 539, https://doi.org/10.1039/b922014c.

[9] S. Albonetti, A. Lolli, V. Morandi, A. Migliori, C. Lucarelli, F. Cavani, Conversion of 5-hydroxymethylfurfural to 2,5-furandicarboxylic acid over Au-based catalysts: Optimization of active phase and metal–support interaction, Appl. Catal. B-Environ. 163 (2015) 520–530, https://doi.org/10.1016/j.apcatb.2014.08.026.

[10] T. Pasini, M. Piccinini, M. Blosi, R. Bonelli, S. Albonetti, N. Dimitratos, J.A. Lopez-Sanchez, M. Sankar, Q. He, C.J. Kiely, G.J. Hutchings, F. Cavani, Selective oxidation of 5-hydroxymethyl-2-furfural using supported gold–copper nanoparticles, Green. Chem. 13 (2011) 2091–2099, https://doi.org/10.1039/C1GC15355B.

[11] S. Albonetti, T. Pasini, A. Lolli, M. Blosi, M. Piccinini, N. Dimitratos, J.A. Lopez-Sanchez, D.J. Morgan, A.F. Carley, G.J. Hutchings, F. Cavani, Selective oxidation of 5-hydroxymethyl-2-furfural over TiO_2-supported gold–copper catalysts prepared from preformed nanoparticles: effect of Au/Cu ratio, Catal. Today 195 (2012) 120–126, https://doi.org/10.1016/j.cattod.2012.05.039.

[12] B.N. Zope, S.E. Davis, R.J. Davis, Influence of reaction conditions on diacid formation during Au-catalyzed oxidation of glycerol and hydroxymethylfurfural, Top. Catal. 55 (2012) 24–32, https://doi.org/10.1007/s11244-012-9777-3.

[13] A. Fujishima, T.N. Rao, D.A. Tryk, Titanium dioxide photocatalysis, J. Photochem. Photobiol. C: Photochem. Rev. 1 (2000) 1–21, https://doi.org/10.1016/s1389-5567(00)00002-2.

[14] A. Fujishima, X. Zhang, D. Tryk, TiO_2 photocatalysis and related surface phenomena, Surf. Sci. Rep. 63 (2008) 515–582, https://doi.org/10.1016/j.surfrep.2008.10.001.

[15] K. Nakata, A. Fujishima, TiO_2 photocatalysis: design and applications, J. Photochem. Photobiol. C: Photochem. Rev. 13 (2012) 169–189, https://doi.org/10.1016/j.jphotochemrev.2012.06.001.

[16] J. Schneider, M. Matsuoka, M. Takeuchi, J. Zhang, Y. Horiuchi, M. Anpo, D. W. Bahnemann, Understanding TiO_2 photocatalysis: mechanisms and materials, Chem. Rev. 114 (2014) 9919–9986, https://doi.org/10.1021/cr5001892.

[17] W. Zhang, H. He, H. Li, L. Duan, L. Zu, Y. Zhai, W. Li, L. Wang, H. Fu, D. Zhao, Visible-light responsive TiO_2-based materials for efficient solar energy utilization, Adv. Energy Mater. 11 (2021), 2003303, https://doi.org/10.1002/aenm.202003303.

[18] L. Jiang, S. Zhou, J. Yang, H. Wang, H. Yu, H. Chen, Y. Zhao, X. Yuan, W. Chu, H. Li, Near-infrared light responsive TiO_2 for efficient solar energy utilization, Adv. Funct. Mater. 32 (2022), 2108977, https://doi.org/10.1002/adfm.202108977.

[19] M. Setvín, U. Aschauer, P. Scheiber, Y.-F. Li, W. Hou, M. Schmid, A. Selloni, U. Diebold, Reaction of O_2 with subsurface oxygen vacancies on TiO_2 anatase (101), Science 341 (2013) 988–991, https://doi.org/10.1126/science.1239879.

[20] L. Hou, M. Zhang, Z. Guan, Q. Li, J. Yang, Effect of annealing ambience on the formation of surface/bulk oxygen vacancies in TiO_2 for photocatalytic hydrogen evolution, Appl. Surf. Sci. 428 (2018) 640–647, https://doi.org/10.1016/j.apsusc.2017.09.144.

[21] X. Bi, G. Du, A. Kalam, D. Sun, Y. Yu, Q. Su, B. Xu, A.G. Al-Sehemi, Tuning oxygen vacancy content in TiO_2 nanoparticles to enhance the photocatalytic performance, Chem. Eng. Sci. 234 (2021), 116440, https://doi.org/10.1016/j.ces.2021.116440.

[22] X. Pan, M.-Q. Yang, X. Fu, N. Zhang, Y.-J. Xu, Defective TiO_2 with oxygen vacancies: synthesis, properties and photocatalytic applications, Nanoscale 5 (2013) 3601, https://doi.org/10.1039/c3nr00476g.

[23] Z. Wang, L. Zang, X. Fan, H. Jia, L. Li, W. Deng, C. Wang, Defect-mediated of Cu@ TiO_2 core–shell nanoparticles with oxygen vacancies for photocatalytic degradation 2,4-DCP under visible light irradiation, Appl. Surf. Sci. 358 (2015) 479–484, https://doi.org/10.1016/j.apsusc.2015.08.051.

[24] Z. Li, S. Wang, J. Wu, W. Zhou, Recent progress in defective TiO_2 photocatalysts for energy and environmental applications, Renew. Sustain. Energy Rev. 156 (2022), 111980, https://doi.org/10.1016/j.rser.2021.111980.

[25] B. Dong, T. Liu, C. Li, F. Zhang, Species, engineering and characterizations of defects in TiO_2-based photocatalyst, Chin. Chem. Lett. 29 (2018) 671–680, https://doi.org/10.1016/j.cclet.2017.12.002.

[26] G. Han, J.Y. Kim, K.-J. Kim, H. Lee, Y.-M. Kim, Controlling surface oxygen vacancies in Fe-doped TiO_2 anatase nanoparticles for superior photocatalytic activities, Appl. Surf. Sci. 507 (2020), 144916, https://doi.org/10.1016/j.apsusc.2019.144916.

[27] V.M. Ramakrishnan, M. Natarajan, A. Santhanam, V. Asokan, D. Velauthapillai, Size controlled synthesis of TiO_2 nanoparticles by modified solvothermal method towards effective photo catalytic and photovoltaic applications, Mater. Res. Bull. 97 (2018) 351–360, https://doi.org/10.1016/j.materresbull.2017.09.017.

[28] D.D. Lee, H.S. Seung, Learning the parts of objects by non-negative matrix factorization, Nature 401 (1999) 788–791, https://doi.org/10.1038/44565.

[29] A.V. Vorontsov, S.V. Tsybulya, Influence of Nanoparticles Size on XRD Patterns for Small Monodisperse Nanoparticles of Cu^0 and TiO_2 Anatase, Ind. Eng. Chem. Res. 57 (2018) 2526–2536, https://doi.org/10.1021/acs.iecr.7b04480.

[30] T. Ungár, Microstructural parameters from X-ray diffraction peak broadening, Scr. Mater. 51 (2004) 777–781, https://doi.org/10.1016/j.scriptamat.2004.05.007.

[31] S.J. Pennycook, C. Li, M. Li, C. Tang, E. Okunishi, M. Varela, Y.-M. Kim, J.H. Jang, Material structure, properties, and dynamics through scanning transmission electron microscopy, J. Anal. Sci. Technol. 9 (2018) 11, https://doi.org/10.1186/s40543-018-0142-4.

[32] Y.-H. Kim, S. Kim, K.-j Kim, C. Kim, J.H. Jang, Y.-M. Kim, H. Lee, Multiscale probing of the influence of the defect-induced variation of oxygen vacancies on the photocatalytic activity of doped ZnO nanoparticles, J. Mater. Chem. A 8 (2020) 25345–25354, https://doi.org/10.1039/D0TA08367D.

[33] B. Bharti, S. Kumar, H.-N. Lee, R. Kumar, Formation of oxygen vacancies and Ti^{3+} state in TiO_2 thin film and enhanced optical properties by air plasma treatment, Sci. Rep. 6 (2016) 32355, https://doi.org/10.1038/srep32355.

[34] W. Göpel, J.A. Anderson, D. Frankel, M. Jaehnig, K. Phillips, J.A. Schäfer, G. Rocker, Surface defects of TiO_2(110): A combined XPS, XAES AND ELS study, Surf. Sci. 139 (1984) 333–346, https://doi.org/10.1016/0039-6028(84)90054-2.

[35] Y. Liu, J. Wang, P. Yang, K. Matras-Postolek, Self-modification of TiO_2 one-dimensional nano-materials by Ti^{3+} and oxygen vacancy using Ti_2O_3 as precursor, RSC Adv. 5 (2015) 61657–61663, https://doi.org/10.1039/c5ra07079a.

[36] A.H. Mamaghani, F. Haghighat, C.-S. Lee, Role of titanium dioxide (TiO_2) structural design/morphology in photocatalytic air purification, Appl. Catal. B: Environ. 269 (2020), 118735, https://doi.org/10.1016/j.apcatb.2020.118735.

[37] W. Wang, C.-H. Lu, Y.-R. Ni, J.-B. Song, M.-X. Su, Z.-Z. Xu, Enhanced visible-light photoactivity of {001} facets dominated TiO_2 nanosheets with even distributed bulk oxygen vacancy and Ti^{3+}, Catal. Commun. 22 (2012) 19–23, https://doi.org/10.1016/j.catcom.2012.02.011.

[38] R. Nawaz, C.F. Kait, H.Y. Chia, M.H. Isa, L.W. Huei, Glycerol-mediated facile synthesis of colored titania nanoparticles for visible light photodegradation of phenolic compounds, Nanomater. 9 (2019) 1586, https://doi.org/10.3390/nano9111586.

[39] M.M. Roessler, E. Salvadori, Principles and applications of EPR spectroscopy in the chemical sciences, Chem. Soc. Rev. 47 (2018) 2534–2553, https://doi.org/10.1039/c6cs00565a.

[40] A. Sarkar, G.G. Khan, The formation and detection techniques of oxygen vacancies in titanium oxide-based nanostructures, Nanoscale 11 (2019) 3414–3444, https://doi.org/10.1039/c8nr09666j.

[41] J. Zhang, L. Zhang, J. Zhang, Z. Zhang, Z. Wu, Effect of surface/bulk oxygen vacancies on the structure and electrochemical performance of TiO_2 nanoparticles, J. Alloy Compd. 642 (2015) 28–33, https://doi.org/10.1016/j.jallcom.2015.04.096.

[42] X. An, Q. Tang, H. Lan, H. Liu, J. Qu, Polyoxometalates/TiO_2 Fenton-like photocatalysts with rearranged oxygen vacancies for enhanced synergetic degradation, Appl. Catal. B: Environ. 244 (2019) 407–413, https://doi.org/10.1016/j.apcatb.2018.11.063.

[43] S. Yurdakal, B.S. Tek, O. Alagöz, V. Augugliaro, V. Loddo, G. Palmisano, L. Palmisano, Photocatalytic selective oxidation of 5-(Hydroxymethyl)-2-furaldehyde to 2,5-furandicarbaldehyde in water by using anatase, rutile, and brookite TiO_2 nanoparticles, ACS Sustain. Chem. Eng. 1 (2013) 456–461, https://doi.org/10.1021/sc300142a.

[44] A. Khan, M. Goepel, A. Kubas, D. Łomot, W. Lisowski, D. Lisovytskiy, A. Nowicka, J.C. Colmenares, R. Gläser, Selective Oxidation of 5-Hydroxymethylfurfural to 2,5-Diformylfuran by Visible Light-Driven Photocatalysis over In Situ Substrate-Sensitized Titania, ChemSusChem 14 (5) (2021) 1351, https://doi.org/10.1002/cssc.202002687.

[45] W.-S. Jang, Y. Jin, Y.-H. Kim, S.-H. Yang, S.J. Kim, J.A. Hong, J. Baik, J. Lee, H. Lee, Y.-M. Kim, Site-selective doping mechanisms for the enhanced photocatalytic activity of tin oxide nanoparticles, Appl. Catal. B: Environ. 305 (2022), 121083, https://doi.org/10.1016/j.apcatb.2022.121083.

[46] Y.I. Kim, M. Jeong, J. Byun, S.-H. Yang, W. Choi, W.-S. Jang, J. Jang, K. Lee, Y. Kim, J. Lee, E. Lee, Y.-M. Kim, Atomic-scale identification of invisible cation vacancies at an oxide homointerface, Mater. Today Phys. 16 (2021), 100302, https://doi.org/10.1016/j.mtphys.2020.100302.

[47] Y.-M. Kim, S.B. Lee, S.H. Oh, Direct observation of an electrically degenerate interface layer in a GaN/sapphire heterostructure, Nanoscale 11 (2019) 8281–8292, https://doi.org/10.1039/C9NR01803D.

[48] A.Y. Borisevich, H.J. Chang, M. Huijben, M.P. Oxley, S. Okamoto, M.K. Niranjan, J. D. Burton, E.Y. Tsymbal, Y.H. Chu, P. Yu, R. Ramesh, S.V. Kalinin, S.J. Pennycook, Suppression of Octahedral Tilts and Associated Changes in Electronic Properties at Epitaxial Oxide Heterostructure Interfaces, Phys. Rev. Lett. 105 (2010), 087204. ⟨https://link.aps.org/doi/10.1103/PhysRevLett.105.087204⟩.

[49] M. Tian, M. Mahjouri-Samani, G. Eres, R. Sachan, M. Yoon, M.F. Chisholm, K. Wang, A.A. Puretzky, C.M. Rouleau, D.B. Geohegan, G. Duscher, Structure and Formation Mechanism of Black TiO_2 Nanoparticles, ACS Nano 9 (2015) 10482–10488, https://doi.org/10.1021/acsnano.5b04712.

[50] M. Cheynet, S. Pokrant, S. Irsen, P. Krüger, New fine structures resolved at the ELNES Ti-L2,3 edge spectra of anatase and rutile: Comparison between experiment and calculation, Ultramicrosc. 110 (2010) 1046–1053, https://doi.org/10.1016/j.ultramic.2010.03.001.

[51] C.-N. Huang, J.-S. Bow, Y. Zheng, S.-Y. Chen, N.J. Ho, P. Shen, Nonstoichiometric titanium oxides via pulsed laser ablation in water, Nanoscale Res. Lett. 5 (2010) 972–985, https://doi.org/10.1007/s11671-010-9591-4.

[52] Y. Li, Y. Yang, X. Shu, D. Wan, N. Wei, X. Yu, M.B.H. Breese, T. Venkatesan, J. M. Xue, Y. Liu, S. Li, T. Wu, J. Chen, From titanium sesquioxide to titanium dioxide: oxidation-induced structural, phase, and property evolution, Chem. Mater. 30 (2018) 4383–4392, https://doi.org/10.1021/acs.chemmater.8b01739.

[53] B. Cao, K. Suenaga, T. Okazaki, H. Shinohara, Production, Isolation, and EELS Characterization of $Ti_2@C_{84}$ Dititanium Metallofullerenes, J. Phys. Chem. B 106 (2002) 9295–9298, https://doi.org/10.1021/jp026013b.

[54] Y. Li, Z.G. Yu, L. Wang, Y. Weng, C.S. Tang, X. Yin, K. Han, H. Wu, X. Yu, L. M. Wong, D. Wan, X.R. Wang, J. Chai, Y.-W. Zhang, S. Wang, J. Wang, A.T.S. Wee, M.B.H. Breese, S.J. Pennycook, T. Venkatesan, S. Dong, J.M. Xue, J. Chen, Electronic-reconstruction-enhanced hydrogen evolution catalysis in oxide polymorphs, Nat. Commun. 10 (2019) 3149, https://doi.org/10.1038/s41467-019-11124-w.

[55] W.T. Hong, K.A. Stoerzinger, Y.-L. Lee, L. Giordano, A. Grimaud, A.M. Johnson, J. Hwang, E.J. Crumlin, W. Yang, Y. Shao-Horn, Charge-transfer-energy-dependent oxygen evolution reaction mechanisms for perovskite oxides, Energy Environ. Sci. 10 (2017) 2190–2200, https://doi.org/10.1039/c7ee02052j.

[56] A. Gloter, C. Ewels, P. Umek, D. Arcon, C. Colliex, Electronic structure of titania-based nanotubes investigated by EELS spectroscopy, Phys. Rev. B 80 (3) (2009) 035413, https://doi.org/10.1103/PhysRevB.80.035413.